

Modified Beer-Lambert law for blood flow

Wesley B. Baker,^{1*} Ashwin B. Parthasarathy,¹ David R. Busch,^{1,2}
Rickson C. Mesquita,³ Joel H. Greenberg,⁴ and A. G. Yodh¹

¹*Dept. Physics and Astronomy, University of Pennsylvania, Philadelphia, PA 19104, USA*

²*Div. of Neurology, Children's Hospital of Philadelphia, Philadelphia, PA 19104, USA*

³*Institute of Physics, University of Campinas, Campinas, SP 13083-859, Brazil*

⁴*Dept. Neurology, University of Pennsylvania, Philadelphia, PA 19104, USA*

*wbaker@sas.upenn.edu

Abstract: We develop and validate a Modified Beer-Lambert law for blood flow based on diffuse correlation spectroscopy (DCS) measurements. The new formulation enables blood flow monitoring from temporal intensity autocorrelation function data taken at single or multiple delay-times. Consequentially, the speed of the optical blood flow measurement can be substantially increased. The scheme facilitates blood flow monitoring of highly scattering tissues in geometries wherein light propagation is diffusive or non-diffusive, and it is particularly well-suited for utilization with pressure measurement paradigms that employ differential flow signals to reduce contributions of superficial tissues.

© 2014 Optical Society of America

OCIS codes: (170.3880) Medical and Biological Imaging; (170.1610) Clinical Applications; (110.4153) Motion estimation and optical flow; (170.2655) Functional monitoring and imaging; (170.3660) Light propagation in tissues; (170.1470) Blood or tissue constituent monitoring; (290.4210) Multiple scattering; (170.5270) Photon density waves; (170.6510) Spectroscopy, tissue diagnostics; (170.6480) Spectroscopy, speckle.

References and links

1. T. Durduran, R. Choe, W. B. Baker, and A. G. Yodh, "Diffuse optics for tissue monitoring and tomography," *Reports on Progress in Physics* **73**, 076701 (2010).
2. A. Villringer and B. Chance, "Non-invasive optical spectroscopy and imaging of human brain function," *Trends in neurosciences* **20**, 435–442 (1997).
3. R. Mesquita, T. Durduran, G. Yu, E. Buckley, M. Kim, C. Zhou, R. Choe, U. Sunar, and A. Yodh, "Direct measurement of tissue blood flow and metabolism with diffuse optics," *Philos. T. Roy. Soc. A* **369**, 4390–4406 (2011).
4. M. Ferrari, M. Muthalib, and V. Quaresima, "The use of near-infrared spectroscopy in understanding skeletal muscle physiology: recent developments," *Philosophical Transactions of the Royal Society A: Mathematical, Physical and Engineering Sciences* **369**, 4577–4590 (2011).
5. D. R. Busch, R. Choe, T. Durduran, and A. G. Yodh, "Towards non-invasive characterization of breast cancer and cancer metabolism with diffuse optics," *PET clinics* **8**, 345–365 (2013).
6. D. R. Leff, O. J. Warren, L. C. Enfield, A. Gibson, T. Athanasiou, D. K. Patten, J. Hebden, G. Z. Yang, and A. Darzi, "Diffuse optical imaging of the healthy and diseased breast: a systematic review," *Breast Cancer Res. Tr.* **108**, 9–22 (2008).
7. T. Hamaoka, K. K. McCully, M. Niwayama, and B. Chance, "The use of muscle near-infrared spectroscopy in sport, health and medical sciences: recent developments," *Philosophical Transactions of the Royal Society A: Mathematical, Physical and Engineering Sciences* **369**, 4591–4604 (2011).
8. D. A. Boas and M. A. Franceschini, "Haemoglobin oxygen saturation as a biomarker: the problem and a solution," *Philosophical Transactions of the Royal Society A: Mathematical, Physical and Engineering Sciences* **369**, 4407–4424 (2011).

9. M. Smith, "Shedding light on the adult brain: a review of the clinical applications of near-infrared spectroscopy," *Philosophical Transactions of the Royal Society A: Mathematical, Physical and Engineering Sciences* **369**, 4452–4469 (2011).
10. H. Obrig and J. Steinbrink, "Non-invasive optical imaging of stroke," *Philosophical Transactions of the Royal Society A: Mathematical, Physical and Engineering Sciences* **369**, 4470–4494 (2011).
11. G. Greisen, T. Leung, and M. Wolf, "Has the time come to use near-infrared spectroscopy as a routine clinical tool in preterm infants undergoing intensive care?" *Philosophical Transactions of the Royal Society A: Mathematical, Physical and Engineering Sciences* **369**, 4440–4451 (2011).
12. L. Meng, A. Gelb, and D. McDonagh, "Changes in cerebral tissue oxygen saturation during anaesthetic-induced hypotension: an interpretation based on neurovascular coupling and cerebral autoregulation," *Anaesthesia* **68**, 736–741 (2013).
13. T. Durduran and A. G. Yodh, "Diffuse correlation spectroscopy for non-invasive, micro-vascular cerebral blood flow measurement," *NeuroImage* **85**, 51–63 (2014).
14. E. M. Buckley, A. B. Parthasarathy, P. E. Grant, A. G. Yodh, and M. A. Franceschini, "Diffuse correlation spectroscopy for measurement of cerebral blood flow: future prospects," *Neurophotonics* **1**, 011009–011009 (2014).
15. D. Boas and A. Yodh, "Spatially varying dynamical properties of turbid media probed with diffusing temporal light correlation," *JOSA A* **14**, 192–215 (1997).
16. D. T. Delpy, M. Cope, P. Van der Zee, S. Arridge, S. Wray, and J. Wyatt, "Estimation of optical pathlength through tissue from direct time of flight measurement," *Physics in medicine and biology* **33**, 1433 (1988).
17. S. R. Arridge, M. Cope, and D. Delpy, "The theoretical basis for the determination of optical pathlengths in tissue: temporal and frequency analysis," *Physics in medicine and biology* **37**, 1531 (1992).
18. M. Hiraoka, M. Firbank, M. Essenpreis, M. Cope, S. Arridge, P. Van Der Zee, and D. Delpy, "A monte carlo investigation of optical pathlength in inhomogeneous tissue and its application to near-infrared spectroscopy," *Physics in medicine and biology* **38**, 1859 (1993).
19. J. Steinbrink, H. Wabnitz, H. Obrig, A. Villringer, and H. Rinneberg, "Determining changes in nir absorption using a layered model of the human head," *Physics in medicine and biology* **46**, 879 (2001).
20. G. Strangman, M. A. Franceschini, and D. A. Boas, "Factors affecting the accuracy of near-infrared spectroscopy concentration calculations for focal changes in oxygenation parameters," *Neuroimage* **18**, 865–879 (2003).
21. F. Fabbri, A. Sassaroli, M. E. Henry, and S. Fantini, "Optical measurements of absorption changes in two-layered diffusive media," *Physics in medicine and biology* **49**, 1183 (2004).
22. R. B. Saager and A. J. Berger, "Direct characterization and removal of interfering absorption trends in two-layer turbid media," *JOSA A* **22**, 1874–1882 (2005).
23. D. Boas, L. Campbell, and A. Yodh, "Scattering and imaging with diffusing temporal field correlations," *Physical review letters* **75**, 1855 (1995).
24. D. Pine, D. Weitz, P. Chaikin, and E. Herbolzheimer, "Diffusing wave spectroscopy," *Physical Review Letters* **60**, 1134 (1988).
25. G. Maret and P. Wolf, "Multiple light scattering from disordered media. the effect of brownian motion of scatterers," *Zeitschrift für Physik B Condensed Matter* **65**, 409–413 (1987).
26. T. Durduran, C. Zhou, B. L. Edlow, G. Yu, R. Choe, M. N. Kim, B. L. Cucchiara, M. E. Putt, Q. Shah, S. E. Kasner, J. H. Greenberg, A. G. Yodh, and J. A. Detre, "Transcranial optical monitoring of cerebrovascular hemodynamics in acute stroke patients," *Optics express* **17**, 3884–3902 (2009).
27. J. P. Culver, T. Durduran, D. Furuya, C. Cheung, J. H. Greenberg, and A. Yodh, "Diffuse optical tomography of cerebral blood flow, oxygenation, and metabolism in rat during focal ischemia," *Journal of cerebral blood flow & metabolism* **23**, 911–924 (2003).
28. Y. Shang, L. Chen, M. Toborek, and G. Yu, "Diffuse optical monitoring of repeated cerebral ischemia in mice," *Optics express* **19**, 20301–20315 (2011).
29. C. G. Favilla, R. C. Mesquita, M. Mullen, T. Durduran, X. Lu, M. N. Kim, D. L. Minkoff, S. E. Kasner, J. H. Greenberg, A. G. Yodh, and J. A. Detre, "Optical bedside monitoring of cerebral blood flow in acute ischemic stroke patients during head-of-bed manipulation," *Stroke* **45**, 1269–1274 (2014).
30. M. N. Kim, T. Durduran, S. Frangos, B. L. Edlow, E. M. Buckley, H. E. Moss, C. Zhou, G. Yu, R. Choe, E. Maloney-Wilensky, R. L. Wolf, M. S. Grady, J. H. Greenberg, J. M. Levine, A. G. Yodh, J. A. Detre, and W. A. Kofke, "Noninvasive measurement of cerebral blood flow and blood oxygenation using near-infrared and diffuse correlation spectroscopies in critically brain-injured adults," *Neurocritical care* **12**, 173–180 (2010).
31. M. N. Kim, B. L. Edlow, T. Durduran, S. Frangos, R. C. Mesquita, J. M. Levine, J. H. Greenberg, A. G. Yodh, and J. A. Detre, "Continuous optical monitoring of cerebral hemodynamics during head-of-bed manipulation in brain-injured adults," *Neurocritical care* **20**, 443–453 (2014).
32. Y. Shang, K. Gurley, and G. Yu, "Diffuse correlation spectroscopy (dcs) for assessment of tissue blood flow in skeletal muscle: Recent progress," *Anatomy & physiology: current research* **3**, 128 (2013).
33. R. C. Mesquita, M. Putt, M. Chandra, G. Yu, X. Xing, S. W. Han, G. Lech, Y. Shang, T. Durduran, C. Zhou, A. G. Yodh, and E. R. Mohler, "Diffuse optical characterization of an exercising patient group with peripheral artery disease," *Journal of biomedical optics* **18**, 057007–057007 (2013).

34. R. C. Mesquita, N. Skuli, M. N. Kim, J. Liang, S. Schenkel, A. J. Majmundar, M. C. Simon, and A. G. Yodh, "Hemodynamic and metabolic diffuse optical monitoring in a mouse model of hindlimb ischemia," *Biomedical optics express* **1**, 1173–1187 (2010).
35. G. Yu, "Near-infrared diffuse correlation spectroscopy in cancer diagnosis and therapy monitoring," *Journal of biomedical optics* **17**, 0109011–0109019 (2012).
36. R. Choe, M. E. Putt, P. M. Carlile, T. Durduran, J. M. Giammarco, D. R. Busch, K. W. Jung, B. J. Czerniecki, J. Tchou, M. D. Feldman, C. Mies, M. A. Rosen, M. D. Schnell, A. DeMichele, and A. G. Yodh, "Optically measured microvascular blood flow contrast of malignant breast tumors," *PloS one* **9**, e99683 (2014).
37. T. Durduran, R. Choe, G. Yu, C. Zhou, J. C. Tchou, B. J. Czerniecki, and A. G. Yodh, "Diffuse optical measurement of blood flow in breast tumors," *Optics letters* **30**, 2915–2917 (2005).
38. U. Sunar, D. Rohrbach, N. Rigual, E. Tracy, K. Keymel, M. T. Cooper, H. Baumann, and B. H. Henderson, "Monitoring photobleaching and hemodynamic responses to hpph-mediated photodynamic therapy of head and neck cancer: a case report," *Optics express* **18**, 14969–14978 (2010).
39. T. Durduran, G. Yu, M. G. Burnett, J. A. Detre, J. H. Greenberg, J. Wang, C. Zhou, and A. G. Yodh, "Diffuse optical measurement of blood flow, blood oxygenation, and metabolism in a human brain during sensorimotor cortex activation," *Optics letters* **29**, 1766–1768 (2004).
40. F. Jaillon, J. Li, G. Dietsche, T. Elbert, and T. Gislser, "Activity of the human visual cortex measured non-invasively by diffusing-wave spectroscopy," *Optics Express* **15**, 6643–6650 (2007).
41. J. Li, M. Ninck, L. Koban, T. Elbert, J. Kissler, and T. Gislser, "Transient functional blood flow change in the human brain measured noninvasively by diffusing-wave spectroscopy," *Optics letters* **33**, 2233–2235 (2008).
42. N. Roche-Labarbe, A. Fenoglio, H. Radhakrishnan, M. Kocienski-Filip, S. A. Carp, J. Dubb, D. A. Boas, P. E. Grant, and M. A. Franceschini, "Somatosensory evoked changes in cerebral oxygen consumption measured non-invasively in premature neonates," *Neuroimage* **85**, 279–286 (2014).
43. V. Jain, E. M. Buckley, D. J. Licht, J. M. Lynch, P. J. Schwab, M. Y. Naim, N. A. Lavin, S. C. Nicolson, L. M. Montenegro, A. G. Yodh, and F. W. Wehrli, "Cerebral oxygen metabolism in neonates with congenital heart disease quantified by mri and optics," *Journal of Cerebral Blood Flow & Metabolism* (2013).
44. G. Yu, "Diffuse correlation spectroscopy (dcs): a diagnostic tool for assessing tissue blood flow in vascular-related diseases and therapies," *Current Medical Imaging Reviews* **8**, 194–210 (2012).
45. P.-A. Lemieux and D. Durian, "Investigating non-gaussian scattering processes by using nth-order intensity correlation functions," *JOSA A* **16**, 1651–1664 (1999).
46. R. C. Haskell, L. O. Svaasand, T.-T. Tsay, T.-C. Feng, M. S. McAdams, and B. J. Tromberg, "Boundary conditions for the diffusion equation in radiative transfer," *JOSA A* **11**, 2727–2741 (1994).
47. J. B. Fishkin and E. Gratton, "Propagation of photon-density waves in strongly scattering media containing an absorbing semi-infinite plane bounded by a straight edge," *JOSA A* **10**, 127–140 (1993).
48. M. S. Patterson, B. Chance, and B. C. Wilson, "Time resolved reflectance and transmittance for the non-invasive measurement of tissue optical properties," *Applied optics* **28**, 2331–2336 (1989).
49. M. Cope, "The development of a near infrared spectroscopy system and its application for non invasive monitoring of cerebral blood and tissue oxygenation in the newborn infants," Ph.D. thesis, University of London (1991).
50. R. Bonner and R. Nossal, "Model for laser doppler measurements of blood flow in tissue," *Applied optics* **20**, 2097–2107 (1981).
51. J. Choi, V. Toronov, U. Wolf, D. Hueber, L. P. Safonova, R. Gupta, C. Polzonetti, M. Wolf, A. Michalos, W. Mantulin, and E. Gratton, "Noninvasive determination of the optical properties of adult brain: near-infrared spectroscopy approach," *Journal of biomedical optics* **9**, 221–229 (2004).
52. B. Hallacoglu, A. Sassaroli, and S. Fantini, "Optical characterization of two-layered turbid media for non-invasive, absolute oximetry in cerebral and extracerebral tissue," *PloS one* **8**, e64095 (2013).
53. O. Pucci, V. Toronov, and K. St Lawrence, "Measurement of the optical properties of a two-layer model of the human head using broadband near-infrared spectroscopy," *Applied optics* **49**, 6324–6332 (2010).
54. L. Gagnon, M. Desjardins, J. Jehanne-Lacasse, L. Bherer, and F. Lesage, "Investigation of diffuse correlation spectroscopy in multi-layered media including the human head," *Optics express* **16**, 15514–15530 (2008).
55. A. Liebert, H. Wabnitz, J. Steinbrink, H. Obrig, M. Möller, R. Macdonald, A. Villringer, and H. Rinneberg, "Time-resolved multidistance near-infrared spectroscopy of the adult head: intracerebral and extracerebral absorption changes from moments of distribution of times of flight of photons," *Applied Optics* **43**, 3037–3047 (2004).
56. T. J. Farrell, M. S. Patterson, and M. Essenpreis, "Influence of layered tissue architecture on estimates of tissue optical properties obtained from spatially resolved diffuse reflectometry," *Applied optics* **37**, 1958–1972 (1998).
57. A. Kienle and T. Glanzmann, "In vivo determination of the optical properties of muscle with time-resolved reflectance using a layered model," *Physics in medicine and biology* **44**, 2689 (1999).
58. R. Choe, T. Durduran, G. Yu, M. J. Nijland, B. Chance, A. G. Yodh, and N. Ramanujam, "Transabdominal near infrared oximetry of hypoxic stress in fetal sheep brain in utero," *Proceedings of the National Academy of Sciences* **100**, 12950–12954 (2003).
59. J. Selb, D. A. Boas, S.-T. Chan, K. C. Evans, E. M. Buckley, and S. A. Carp, "Sensitivity of near-infrared

- spectroscopy and diffuse correlation spectroscopy to brain hemodynamics: simulations and experimental findings during hypercapnia,” *Neurophotonics* **1**, 015005–015005 (2014).
60. I. Vogiatzis, Z. Louvaris, H. Habazettl, D. Athanasopoulos, V. Andrianopoulos, E. Cherouveim, H. Wagner, C. Roussos, P. D. Wagner, and S. Zakynthinos, “Frontal cerebral cortex blood flow, oxygen delivery and oxygenation during normoxic and hypoxic exercise in athletes,” *The Journal of physiology* **589**, 4027–4039 (2011).
 61. A. A. Middleton and D. S. Fisher, “Discrete scatterers and autocorrelations of multiply scattered light,” *Physical Review B* **43**, 5934 (1991).
 62. D. A. Weitz and D. J. Pine, *Dynamic light scattering: the method and some applications* (Oxford University Press, USA, 1993), vol. 49, chap. Diffusing-wave spectroscopy.
 63. C. Zhou, G. Yu, D. Furuya, J. Greenberg, A. Yodh, and T. Durduran, “Diffuse optical correlation tomography of cerebral blood flow during cortical spreading depression in rat brain,” *Optics express* **14**, 1125–1144 (2006).
 64. B. Hallacoglu, A. Sassaroli, M. Wysocki, E. Guerrero-Berrea, M. S. Beeri, V. Haroutunian, M. Shaul, I. H. Rosenberg, A. M. Troen, and S. Fantini, “Absolute measurement of cerebral optical coefficients, hemoglobin concentration and oxygen saturation in old and young adults with near-infrared spectroscopy,” *Journal of biomedical optics* **17**, 0814061–0814068 (2012).
 65. S. Ijichi, T. Kusaka, K. Isobe, K. Kawada, T. Imai, S. Itoh, F. Islam, K. Okubo, H. Okada, and M. Namba, “Quantification of cerebral hemoglobin as a function of oxygenation using near-infrared time-resolved spectroscopy in a piglet model of hypoxia,” *Journal of biomedical optics* **10**, 024026–0240269 (2005).
 66. E. A. Mellon, R. S. Beesam, M. A. Elliott, and R. Reddy, “Mapping of cerebral oxidative metabolism with mri,” *Proceedings of the National Academy of Sciences* **107**, 11787–11792 (2010).
 67. F. Scholkmann, S. Kleiser, A. J. Metz, R. Zimmermann, J. Mata Pavia, U. Wolf, and M. Wolf, “A review on continuous wave functional near-infrared spectroscopy and imaging instrumentation and methodology,” *Neuroimage* **85**, 6–27 (2014).
 68. S. Lloyd-Fox, A. Blasi, and C. Elwell, “Illuminating the developing brain: the past, present and future of functional near infrared spectroscopy,” *Neuroscience & Biobehavioral Reviews* **34**, 269–284 (2010).
 69. M. Ferrari and V. Quaresima, “A brief review on the history of human functional near-infrared spectroscopy (fnirs) development and fields of application,” *Neuroimage* **63**, 921–935 (2012).
 70. D. R. Leff, F. Orihuela-Espina, C. E. Elwell, T. Athanasiou, D. T. Delpy, A. W. Darzi, and G.-Z. Yang, “Assessment of the cerebral cortex during motor task behaviours in adults: a systematic review of functional near infrared spectroscopy (fnirs) studies,” *NeuroImage* **54**, 2922–2936 (2011).
 71. B. Ackerson, R. Dougherty, N. Reguigui, and U. Nobbmann, “Correlation transfer-application of radiative transfer solution methods to photon correlation problems,” *Journal of thermophysics and heat transfer* **6**, 577–588 (1992).
 72. R. Dougherty, B. Ackerson, N. Reguigui, F. Dorri-Nowkoorani, and U. Nobbmann, “Correlation transfer: development and application,” *Journal of Quantitative Spectroscopy and Radiative Transfer* **52**, 713–727 (1994).
 73. F. Jaillon, S. E. Skipetrov, J. Li, G. Dietsche, G. Maret, and T. Gisler, “Diffusing-wave spectroscopy from head-like tissue phantoms: influence of a non-scattering layer,” *Optics express* **14**, 10181–10194 (2006).
 74. E. Okada and D. T. Delpy, “Near-infrared light propagation in an adult head model. i. modeling of low-level scattering in the cerebrospinal fluid layer,” *Applied optics* **42**, 2906–2914 (2003).
 75. A. Custer, W. M. Wells Iii, A. H. Barnett, E. Hillman, and D. A. Boas, “Effective scattering coefficient of the cerebral spinal fluid in adult head models for diffuse optical imaging,” *Applied optics* **45**, 4747–4755 (2006).
 76. S. L. Jacques, “Optical properties of biological tissues: a review,” *Physics in medicine and biology* **58**, R37 (2013).
 77. D. R. Busch, R. Choe, T. Durduran, D. H. Friedman, W. B. Baker, A. D. Maidment, M. A. Rosen, M. D. Schnall, and A. G. Yodh, “Blood flow reduction in breast tissue due to mammographic compression,” *Academic radiology* **21**, 151–161 (2014).
 78. J. Dong, R. Bi, J. H. Ho, P. S. Thong, K.-C. Soo, and K. Lee, “Diffuse correlation spectroscopy with a fast fourier transform-based software autocorrelator,” *Journal of biomedical optics* **17**, 0970041–0970049 (2012).
 79. K. Schatzel, *Dynamic light scattering: the method and some applications* (Oxford University Press, USA, 1993), vol. 49, chap. Single photon correlation techniques.
 80. Y. Shang, T. Symons, T. Durduran, A. G. Yodh, and G. Yu, “Effects of muscle fiber motion on diffuse correlation spectroscopy blood flow measurements during exercise,” *Biomedical optics express* **1**, 500–511 (2010).
 81. E. Okada and D. T. Delpy, “Near-infrared light propagation in an adult head model. ii. effect of superficial tissue thickness on the sensitivity of the near-infrared spectroscopy signal,” *Applied optics* **42**, 2915–2922 (2003).
 82. A. Sassaroli, F. Martelli, and S. Fantini, “Perturbation theory for the diffusion equation by use of the moments of the generalized temporal point-spread function. i. theory,” *JOSA A* **23**, 2105–2118 (2006).
 83. R. C. Mesquita, S. S. Schenkel, D. L. Minkoff, X. Lu, C. G. Favilla, P. M. Vora, D. R. Busch, M. Chandra, J. H. Greenberg, J. A. Detre, and A. G. Yodh, “Influence of probe pressure on the diffuse correlation spectroscopy blood flow signal: extra-cerebral contributions,” *Biomedical optics express* **4**, 978–994 (2013).
 84. S. Fantini, D. Hueber, M. A. Franceschini, E. Gratton, W. Rosenfeld, P. G. Stubblefield, D. Maulik, and M. R. Stankovic, “Non-invasive optical monitoring of the newborn piglet brain using continuous-wave and frequency-

- domain spectroscopy,” *Physics in medicine and biology* **44**, 1543 (1999).
85. E. M. Buckley, “Cerebral hemodynamics in high-risk neonates probed by diffuse optical spectroscopies (chapter 4.2),” Ph.D. thesis, University of Pennsylvania (2011).
 86. M. N. Kim, “Applications of hybrid diffuse optics for clinical management of adults after brain injury (chapter 3),” Ph.D. thesis, University of Pennsylvania (2013).
-

1. Introduction

Diffuse optical techniques, such as near-infrared or diffuse optical spectroscopy (DOS, NIRS) and diffuse correlation spectroscopy (DCS), have been employed with remarkable success over the last two decades to probe hemodynamic processes in highly scattering tissues such as human brain, muscle and breast [1–11]. In total, this research has discovered new indicators of tissue function and health that are proving to be clinically relevant [6–14]. The most basic DOS/NIRS instrument measures diffuse reflectance from tissue as a function of input wavelength, and thereby derives the concentration of tissue chromophores and contrast agents, including oxy- and deoxy-hemoglobin (HbO_2 , Hb), and changes thereof. Diffuse correlation spectroscopy (DCS), by contrast, is a more recently developed optical technique that utilizes the temporal intensity fluctuations of multiply scattered light in order to quantify microvascular blood flow in highly scattering tissues [13–15]. Like DOS/NIRS, the DCS method is non-invasive and penetrates tissue deeply, but DCS also offers the possibility to directly measure the “blood flow” contribution to tissue hemodynamics, continuously and at the bedside.

In this contribution we develop and validate a Modified Beer-Lambert law for measurement of blood flow based on the DCS technique. This method linearly relates measured changes of a newly-defined “DCS optical density” to the variation of tissue blood flow, tissue scattering, and tissue absorption. The novel algorithm parallels the DOS/NIRS Modified Beer-Lambert law, but it has interesting differences that should be useful for applications that require continuous monitoring of blood flow.

Traditional optical spectroscopy measures the attenuation of light traveling through a sample as a function of wavelength. In cases where scattering is negligible, i.e., in which the reduced scattering coefficient (μ'_s) is zero, light attenuation is dominated by absorption, and the transmitted intensity ($I(t)$) at time t is related to the sample absorption coefficient (μ_a) via the Beer-Lambert law: $I(t) = I_s \exp[-\mu_a \rho]$. Here, I_s is the incident light intensity, and ρ is the sample length. The sample optical density (OD) is defined as the negative logarithm of the ratio of transmitted to incident light intensity; it is proportional to the absorption coefficient, i.e., $OD \equiv -\log[I(t)/I_s] = \mu_a \rho$. When scattering within the sample is significant, however, then light attenuation is affected by both absorption and scattering. In these situations, the effects of scattering become tangled with those of absorption [1]. Typically, the photon trajectories through tissue samples with significant scattering are well approximated as random walks, and the average length of a photon path through tissue is much greater than the straight-line distance between source and detector.

Among the most widely used approaches for analysis of such DOS/NIRS reflectance signals is the so-called Modified Beer-Lambert law [16–18]. The Modified Beer-Lambert paradigm is an algorithm that derives changes in tissue optical properties based on continuous-wave (CW) diffuse optical intensity measurements. In its simplest form, the scheme relates differential light transmission changes (in any geometry) to differential changes in tissue absorption. Here the term differential refers to a comparison between a baseline state and a perturbed state. In essence, the Modified Beer-Lambert law accounts for tissue scattering by using the mean pathlength traveled by photons through the highly scattering sample as a best estimate for the actual photon pathlengths. The mean pathlength provides a natural constant of proportionality between the measured differential intensity and the sample’s differential absorption.

The Modified Beer-Lambert law is readily derived from the first order Taylor expansion of the optical density: $OD \approx OD^0 + (\partial OD^0 / \partial \mu_a) \Delta \mu_a + (\partial OD^0 / \partial \mu_s') \Delta \mu_s'$, wherein the partial derivatives are evaluated in the “baseline” state ($\mu_a = \mu_a^0, \mu_s' = \mu_s'^0$), $OD^0 \equiv -\log[I^0/I_s]$ is the baseline optical density, and the differential changes in absorption and scattering are denoted by $\Delta \mu_a \equiv \mu_a(t) - \mu_a^0$ and $\Delta \mu_s' \equiv \mu_s'(t) - \mu_s'^0$, respectively. Note that the superscript “0” indicates baseline. Within this approximation, the change in optical density from baseline is

$$\Delta OD = -\log\left(\frac{I(t)}{I^0}\right) \approx \langle L \rangle \Delta \mu_a(t) + \left(\frac{\mu_a^0}{\mu_s'^0}\right) \langle L \rangle \Delta \mu_s'(t) \approx \langle L \rangle \Delta \mu_a(t). \quad (1)$$

Here, $\langle L \rangle \equiv \partial OD^0 / \partial \mu_a$ is the so-called differential pathlength, which is approximately the mean pathlength that diffusing photons travel through the medium from source to detector [17]. Notice that whereas the traditional Beer-Lambert law relates *absolute* optical densities to *absolute* absorption coefficients, the Modified Beer-Lambert law (Eq. (1)) relates *differential changes* in the optical density to *differential changes* in the absorption coefficient. This algorithm has proved useful for many reasons; it is simple, fast, and fairly accurate. To date the Modified Beer-Lambert algorithms have been applied predominantly to monitor hemoglobin concentration changes in the brain; within this context, it has been extended from semi-infinite geometries to two-layer geometries [18–22] characteristic of many tissues, especially the human head.

Herein, we derive a Modified Beer-Lambert law for measurement of blood flow based on the DCS technique in turbid tissues, and we validate the approach. The Modified Beer-Lambert law for blood flow linearly relates changes in tissue blood flow, tissue scattering, and tissue absorption to variation of a newly-defined “DCS optical density” (OD_{DCS}). The new algorithm parallels the DOS/NIRS Modified Beer-Lambert law, since the transport of both the light fluence rate and the electric field autocorrelation function through highly scattering tissues is well approximated as a diffusive process [1]. Importantly, however, the diffusion equation for the DCS signal is sensitive to the movement of red blood cells in tissue microvasculature, and therefore the precise form of the Modified Beer-Lambert law for blood flow is different from the traditional (DOS/NIRS) form. The weighting factors in the new law, for example, are not as easily interpreted in terms of a mean pathlength. We derive general theoretical results for measurement of flow changes in any geometry, and then we obtain specific expressions for two common tissue models: homogeneous semi-infinite turbid media and two-layer turbid media. We demonstrate the new approach with simulations and with an *in-vivo* pig-brain experiment. In the future, we expect the Modified Beer-Lambert law for flow to offer increased DCS measurement speed, simpler DCS instrumentation, and, importantly, access to novel measurement paradigms based on differential blood flow signals. Ultimately, these developments should lead to improvements in characterization of cerebral flow and metabolism, with concomitant clinical impact.

2. Diffuse correlation spectroscopy

Diffuse correlation spectroscopy (DCS) employs NIR light to non-invasively measure tissue blood flow. Since early work with *in-vitro* phantoms and *in-vivo* tissues [15, 23–25], it has been used in a variety of clinical applications such as stroke [26–29], brain injury [30, 31], muscle disease [32–34], cancer [35–38], and in functional activation studies [39–42]. In addition, the DCS blood flow index has been successfully validated against a plethora of gold-standard techniques [3, 43]. Several recent reviews highlight the theory, implementation and applications of DCS [1, 3, 13, 14, 44], and therefore our background discussion will be brief.

DCS detects tissue blood flow using speckle correlation techniques. It measures the temporal intensity fluctuations of coherent NIR light that has scattered from moving particles (red blood

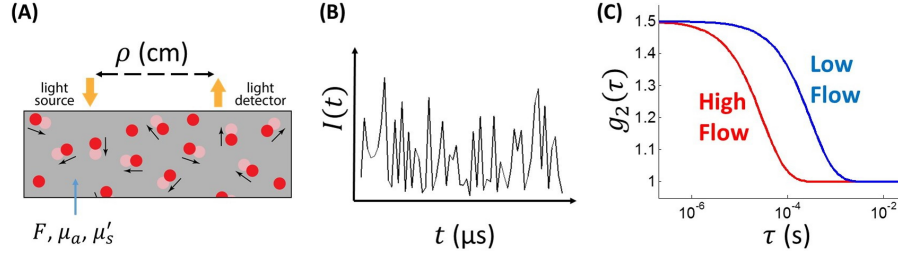


Fig. 1. (A) Schematic for blood flow monitoring in a homogeneous, semi-infinite turbid tissue (see text for details). Blood cell (e.g., red disks at time t and light-red disks at time $t + \tau$) motion induces temporal fluctuations in the scattered light intensity, $I(t)$, at the light detector (panel B). These intensity fluctuations are characterized by the normalized intensity autocorrelation function ($g_2(\tau)$). (C) The decay of the intensity autocorrelation function curves is related to tissue blood flow.

cells) in tissue (Fig. 1(A)). These temporal fluctuations (Fig. 1(B)) are quantified by computing the normalized intensity temporal autocorrelation function at multiple delay-times, τ , i.e., we compute $g_2(\tau) \equiv \langle I(t)I(t+\tau) \rangle / \langle I(t) \rangle^2$, where $I(t)$ is the intensity of the detected light at time t , and the angular brackets, $\langle \rangle$, represent time-averages. An index of tissue blood flow is then provided by the temporal decay of the detected intensity autocorrelation function (Fig. 1(C)).

Formally, the transport of the electric field ($\mathbf{E}(t)$) autocorrelation function, $G_1(\tau) \equiv \langle \mathbf{E}^*(t) \cdot \mathbf{E}(t+\tau) \rangle$, is well modeled by the so-called correlation diffusion equation [15,23], which can be solved analytically or numerically for tissue geometries of interest [1,15]. Tissue blood flow can be ascertained by fitting the solution for the normalized electric field autocorrelation function, $g_1(\tau) = G_1(\tau)/G_1(\tau=0)$, to the measured (normalized) intensity autocorrelation function via the Siegert relation [45]: $g_2(\tau) = 1 + \beta |g_1(\tau)|^2$, where β is a constant determined primarily by the experimental collection optics.

As an example, for the simple case of point illumination and point detection on the surface of semi-infinite homogeneous tissue (Fig. 1(A)) with absorption coefficient μ_a , reduced scattering coefficient μ'_s , and tissue blood flow index F , the solution to the correlation diffusion equation is [1,15]:

$$G_1(\tau) = \frac{3}{4\pi\ell_{tr}} \left[\frac{\exp(-K(\tau)r_1)}{r_1} - \frac{\exp(-K(\tau)r_b)}{r_b} \right]. \quad (2)$$

Here, $K(\tau) = [3\mu_a(\mu_a + \mu'_s)(1 + 2\mu'_s k_0^2 F \tau / \mu_a)]^{1/2}$, $r_1 = (\ell_{tr}^2 + \rho^2)^{1/2}$, $r_b = [(2z_b + \ell_{tr})^2 + \rho^2]^{1/2}$, ρ is the source-detector separation, and $\ell_{tr} = 1/(\mu_a + \mu'_s)$. Further, $k_0 = 2\pi n/\lambda$ is the magnitude of the light wave vector in the medium, and $z_b = 2\ell_{tr}(1 + R_{eff})/(3(1 - R_{eff}))$, where R_{eff} is the effective reflection coefficient that accounts for the mismatch between the index of refraction of tissue (n) and the index of refraction of the non-scattering medium bounding the tissue (n_{out}), such as air [46].

A standard approach for blood flow monitoring with DCS in this geometry is to derive $g_1(\tau)$ from measurements of $g_2(\tau)$ via the Siegert relation. Then, the semi-infinite correlation diffusion solution (Eq. (2)) is fit to $g_1(\tau)$ using a nonlinear minimization algorithm, and an estimate of the blood flow index (F) is obtained from the fit.

3. Modified Beer-Lambert law for flow

We now develop a ‘‘Modified Beer-Lambert law’’ for tissue blood flow based on the DCS measurement. The first step in this process is to define a ‘‘DCS optical density’’ (OD_{DCS}), in analogy with the OD for DOS/NIRS. For source-detector separation ρ and delay-time τ , we

define the DCS optical density as: $OD_{DCS}(\tau, \rho) \equiv -\log(g_2(\tau, \rho) - 1)$. Notice that in addition to delay time and source-detector separation, the DCS optical density also implicitly depends on tissue absorption, scattering, and blood flow (e.g, Eq. (2)).

3.1. DCS Modified Beer-Lambert law for homogeneous tissue

We first derive a general expression for homogeneous tissue characterized by a blood flow index, F , an absorption coefficient, μ_a , and a reduced scattering coefficient, μ'_s . The DCS Modified Beer-Lambert law is obtained by truncating the Taylor series expansion of the DCS optical density to first order in F , μ_a , and μ'_s , i.e.,

$$OD_{DCS}(\tau, \rho) \approx OD_{DCS}^0(\tau, \rho) + \frac{\partial OD_{DCS}^0}{\partial F} \Delta F + \frac{\partial OD_{DCS}^0}{\partial \mu_a} \Delta \mu_a + \frac{\partial OD_{DCS}^0}{\partial \mu'_s} \Delta \mu'_s. \quad (3)$$

Here, $OD_{DCS}^0(\tau, \rho) \equiv -\log(g_2^0(\tau, \rho) - 1)$ is the “baseline” DCS optical density with a baseline blood flow index, F^0 , and with baseline optical properties μ_a^0 and $\mu'_s{}^0$. Correspondingly, $OD_{DCS}(\tau, \rho) \equiv -\log(g_2(\tau, \rho) - 1)$ is the DCS optical density for the intensity autocorrelation function in the “perturbed” state with blood flow index F , and with optical properties μ_a and μ'_s . The differential changes from baseline of tissue blood flow, absorption, and scattering are $\Delta F \equiv F - F^0$, $\Delta \mu_a \equiv \mu_a - \mu_a^0$, and $\Delta \mu'_s \equiv \mu'_s - \mu'_s{}^0$, respectively.

Comparing Eq. (3) with Eq. (1), the DCS analogues of the differential pathlength are $d_F(\tau, \rho) \equiv \partial OD_{DCS}^0 / \partial F$, $d_a(\tau, \rho) \equiv \partial OD_{DCS}^0 / \partial \mu_a$, and $d_s(\tau, \rho) \equiv \partial OD_{DCS}^0 / \partial \mu'_s$, which can be estimated analytically or numerically using the correlation diffusion model applied to the appropriate geometry (*Appendix 1*). All three of these weighting factors depend on τ and ρ , on tissue geometry, and on the baseline parameters F^0 , μ_a^0 , and $\mu'_s{}^0$. Rearranging Eq. (3), we arrive at the “DCS” Modified Beer-Lambert law for homogeneous tissue:

$$\Delta OD_{DCS}(\tau, \rho) = -\log\left(\frac{g_2(\tau, \rho) - 1}{g_2^0(\tau, \rho) - 1}\right) \approx d_F(\tau, \rho) \Delta F + d_a(\tau, \rho) \Delta \mu_a + d_s(\tau, \rho) \Delta \mu'_s. \quad (4)$$

If the blood flow and optical properties change only slightly, then the perturbation in the DCS optical density is small, and the first order expansion (Eq. (3)) is a good approximation. Notice, however, that even for large tissue hemodynamic changes, ΔOD_{DCS} can still be small at *short delay-times*, because in this limit, d_F , d_a , and d_s are close to zero (Fig. 2). Analytical and numerical computation of these weighting factors (d_F , d_a , d_s) are described and given in *Appendix 1*.

Eq. (4) is a general result that describes the change in DCS optical density for homogeneous tissue. For a given tissue/measurement geometry, the change in blood flow can be computed by evaluating the weighting factors for the geometry in question, and then inserting these resultant weighting factors into Eq. (4).

3.2. DCS Modified Beer-Lambert law for homogeneous semi-infinite geometries

It is straightforward to evaluate the weighting factors in Eq. (4) for the special case of the homogeneous semi-infinite geometry (Fig. 1(A)). Recall from Eq. (2) that the normalized electric field autocorrelation function is

$$g_1(\tau) = \frac{\exp(-K(\tau)r_1)/r_1 - \exp(-K(\tau)r_b)/r_b}{\exp(-K_0 r_1)/r_1 - \exp(-K_0 r_b)/r_b}, \quad (5)$$

where $K(\tau)$, r_1 , and r_b are as defined in *Section 2*, and $K_0 = K(\tau = 0) = [3\mu_a(\mu_a + \mu'_s)]^{1/2}$. The multiplicative weighting factors in the semi-infinite geometry can be computed from

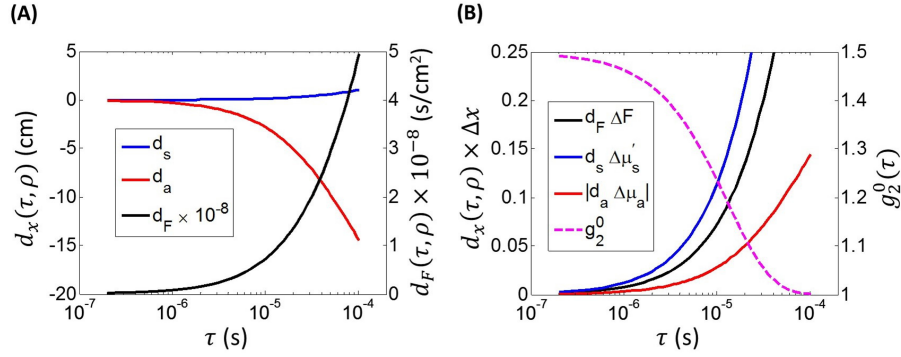


Fig. 2. (A) The semi-infinite multiplicative weighting factors (see Eq. (4)) for tissue scattering (d_s), for tissue absorption (d_a), and for tissue blood flow (d_F , right vertical-axis). They are plotted as a function of the correlation time, τ , for source-detector separation, $\rho = 3$ cm, and optical wavelength, $\lambda = 785$ nm, given a typical set of cerebral tissue properties, i.e., $\mu_a^0 = 0.1$ cm $^{-1}$, $\mu_s^0 = 8$ cm $^{-1}$, $F^0 = 10^{-8}$ cm 2 /s, $n = 1.4$, $n_{out} = 1$. (B) The semi-infinite DCS Modified Beer-Lambert components $d_F(\tau, \rho)\Delta F$, $d_s(\tau, \rho)\Delta\mu'_s$, and $|d_a(\tau, \rho)\Delta\mu_a|$, plotted as a function of τ for a 10% increase in blood flow, tissue scattering, and tissue absorption, respectively. On the right vertical-axis is the intensity autocorrelation function, $g_2^0(\tau)$, for $\beta = 0.5$. Given the same fractional change in tissue properties, the DCS signal is most sensitive to scattering changes, followed by flow changes, and finally absorption changes. In many applications, however, the scattering changes associated with hemodynamic perturbations are negligible, e.g., such as an increase in blood flow and blood volume; in these situations the scattering component can be neglected (see text).

substitution of Eq. (5) into Equations (A.1) and (A.2), e.g.,

$$d_F(\tau, \rho) = \frac{6\mu_s^0 (\mu_s^0 + \mu_a^0) k_0^2 \tau}{K^0(\tau)} \left[\frac{\exp(-K^0(\tau)r_1^0) - \exp(-K^0(\tau)r_b^0)}{\exp(-K^0(\tau)r_1^0)/r_1^0 - \exp(-K^0(\tau)r_b^0)/r_b^0} \right]. \quad (6)$$

In Fig. 2, d_F , d_a , and d_s in the semi-infinite geometry are plotted as a function of τ using typical tissue properties. Note that all three weighting factors are small in magnitude for short delay-times. Further, the weighting factor for absorption is negative, i.e., an increase in absorption is accompanied by a decrease in the DCS flow optical density (compared to baseline), and the weighting factors for flow and scattering are positive.

Because the weighting factors are small at shorter delay-times (Fig. 2), the DCS optical density perturbation will also be small, which in turn implies higher accuracy for the DCS Modified Beer-Lambert law (Eq. (4)). Ideally, in the semi-infinite geometry, the delay-times used for Eq. (4) should satisfy the limits $2\mu_s^0 k_0^2 F^0 \tau / \mu_a \ll 1$ and $2\mu_s^0 k_0^2 F^0 \tau / \mu_a^0 \ll 1$ to obtain the most quantitatively accurate results (see Appendix 2). From our experience with simulations and real data, we have found that a good “rule of thumb” for accurately using Eq. (4) is to utilize data wherein $g_1^0(\tau) > 0.5$, which corresponds to $g_2^0(\tau) > 1.1$ for $\beta = 0.5$.

Figure 2(B) shows that for the same fractional changes (10%) in blood flow, tissue scattering, and tissue absorption, the change in DCS optical density is greatest due to scattering, followed by flow; changes in absorption have the least influence on the DCS signal. In practice, concurrent frequency-domain or time-domain DOS/NIRS can (and should) be employed to directly measure tissue absorption and scattering [1, 47, 48] and account for their effects. This mode of operation, i.e., with concurrent optical measurements, is always desirable. Importantly, however, the tissue scattering changes that typically accompany hemodynamic concentration variations are often negligible; the origin of hemodynamic variation is blood, but the origin

of tissue scattering is predominantly from interfaces between cells and the extracellular space, or between cellular cytoplasm and cellular organelles [49]. The tissue blood volume (BV) is typically a small fraction ($< 4\%$) of the tissue volume (V_{tissue}), and red blood cells account for only a small fraction of the tissue scattering [50]. Scattering from blood ($\mu'_{s,\text{blood}}$) is proportional to the blood volume, i.e., $\mu'_{s,\text{blood}} = \sigma_{\text{blood}}(1 - g)(Hct/V_{RBC})(BV/V_{\text{tissue}})$, where σ_{blood} , g , and V_{RBC} are the scattering cross-section, scattering anisotropy factor, and volume of a red blood cell, and Hct is the hematocrit. Consequentially, while tissue scattering can change with variation in blood volume, the magnitude of this change is often quite small, because the overall volume fraction of blood in tissue is quite small.

As an example, the finger tapping functional task induces a localized increase in cerebral blood volume of roughly 10% [39], which corresponds approximately to a 10% increase in scattering from blood. However, the fractional increase in total scattering is much less than 10% because blood only accounts for a small fraction of tissue scattering. If we assume that blood accounts for less than 5% of total tissue scattering [49], then the tissue scattering change due to increased blood volume from finger tapping is less than 0.5%.

3.3. DCS Modified Beer-Lambert law for heterogeneous tissue

Tissue is perhaps too often approximated to be optically homogeneous for hemodynamic monitoring, an approach which has the advantage of simplicity. Realistically, however, tissue is heterogeneous; it contains multiple compartments with different optical properties due to vasculature, fat, and bone. Often these regions arise as “layers” below the tissue surface such as scalp, skull, and cortex. Under these conditions, a Taylor series expansion of the DCS optical density can also be used to derive the DCS Modified Beer-Lambert law for heterogeneous media. Assuming that the heterogeneous tissue can be divided into N piecewise homogeneous regions, then the first-order Taylor series expansion of the DCS optical density is

$$OD_{DCS}(\tau, \rho) \approx OD_{DCS}^0(\tau, \rho) + \sum_{k=1}^N \left[\frac{\partial OD_{DCS}^0}{\partial F_k} \Delta F_k + \frac{\partial OD_{DCS}^0}{\partial \mu_{a,k}} \Delta \mu_{a,k} + \frac{\partial OD_{DCS}^0}{\partial \mu'_{s,k}} \Delta \mu'_{s,k} \right]. \quad (7)$$

Here, F_k , $\mu_{a,k}$, and $\mu'_{s,k}$ denote the blood flow index, tissue absorption, and tissue scattering for the k th homogeneous region in the tissue, respectively, and $\Delta F_k \equiv F_k - F_k^0$, $\Delta \mu_{a,k} \equiv \mu_{a,k} - \mu_{a,k}^0$, and $\Delta \mu'_{s,k} \equiv \mu'_{s,k} - \mu_{s,k}^0$ denote the changes in these parameters from baseline. Rearranging Eq. (7), the DCS Modified Beer-Lambert law for heterogeneous media is:

$$-\log \left(\frac{g_2(\tau, \rho) - 1}{g_2^0(\tau, \rho) - 1} \right) \approx \sum_{k=1}^N [d_{F,k}(\tau, \rho) \Delta F_k + d_{a,k}(\tau, \rho) \Delta \mu_{a,k} + d_{s,k}(\tau, \rho) \Delta \mu'_{s,k}], \quad (8)$$

where $\{d_{F,k} \equiv \partial OD_{DCS}^0 / \partial F_k, d_{a,k} \equiv \partial OD_{DCS}^0 / \partial \mu_{a,k}, d_{s,k} \equiv \partial OD_{DCS}^0 / \partial \mu'_{s,k}\}$ are DCS analogues of the partial pathlengths from DOS/NIRS [18]. These multiplicative weighting factors depend on tissue geometry, on the baseline tissue properties, i.e., $\{F_k^0, \mu_{a,k}^0, \mu_{s,k}^0\}$, and on τ and ρ . They account for the relative importance of the various regional hemodynamic changes in the DCS optical density perturbation, and they can be estimated in the same manner as described in *Appendix 1*.

3.4. DCS Modified Beer-Lambert law for two-layer media

The simplest heterogeneous model for tissue is the two-layer geometry, an important special case (Fig. 3). Researchers have used this geometry in order to distinguish cerebral tissue from extra-cerebral tissue in optical measurements of the head [22, 39, 51–55], to model tissue burns [15], to distinguish skin from fat/muscle [56, 57], to distinguish fetal from maternal tissues [58],

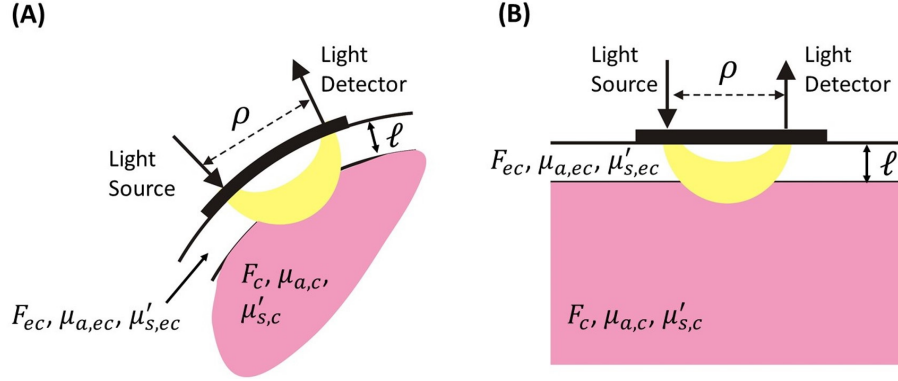


Fig. 3. (A) Two-layer tissue model of the head and (B) parallel plane two-layer tissue geometry.

and in other applications. For cerebral applications, the two-layer geometry is comprised of a semi-infinite bottom layer (i.e., corresponding to the cortical regions of the brain) with a distinct blood flow index, absorption coefficient, and scattering coefficient of F_c , $\mu_{a,c}$, and $\mu'_{s,c}$, respectively, and a superficial top layer (i.e., corresponding to extra-cerebral scalp and skull tissue) with thickness ℓ , and distinct tissue properties denoted by F_{ec} , $\mu_{a,ec}$, and $\mu'_{s,ec}$.

The two-layer DCS Modified Beer-Lambert law is the special case of Eq. (8) for $N = 2$ piecewise homogeneous (layered) regions, i.e.,

$$\Delta OD_{DCS}(\tau, \rho) = -\log\left(\frac{g_2(\tau, \rho) - 1}{g_2^0(\tau, \rho) - 1}\right) \approx d_{F,c}(\tau, \rho)\Delta F_c + d_{F,ec}(\tau, \rho)\Delta F_{ec} + d_{a,c}(\tau, \rho)\Delta\mu_{a,c} + d_{a,ec}(\tau, \rho)\Delta\mu_{a,ec} + d_{s,c}(\tau, \rho)\Delta\mu'_{s,c} + d_{s,ec}(\tau, \rho)\Delta\mu'_{s,ec}. \quad (9)$$

Again, the multiplicative weighting factors, $d_{F,i} \equiv \partial OD_{DCS}^0 / \partial F_i$, $d_{a,i} \equiv \partial OD_{DCS}^0 / \partial \mu_{a,i}$, and $d_{s,i} \equiv \partial OD_{DCS}^0 / \partial \mu'_{s,i}$ (with subscript i denoting c (cerebral) or ec (extra-cerebral)), indicate the relative sensitivity of the DCS optical density variation to cerebral versus extra-cerebral hemodynamic changes. All six parameters depend on delay-time τ , source-detector separation ρ , top layer thickness ℓ , and baseline tissue properties F_c^0 , F_{ec}^0 , $\mu_{a,c}^0$, $\mu_{a,ec}^0$, $\mu_{s,c}^0$, and $\mu_{s,ec}^0$. They can be computed by numerically taking the appropriate derivatives of the two-layer solution to the correlation diffusion equation. For the parallel plane two-layer geometry (Fig. 3(B)), the solution is [15, 54]:

$$g_1(\tau) = G_1(\tau)/G_1(0),$$

$$G_1(\tau) = \frac{1}{2\pi} \int_0^\infty \tilde{G}_1(\tau) s J_0(s\rho) ds,$$

$$\tilde{G}_1(\tau) = \frac{\sinh[\kappa_{ec}(z_b + z_0)]}{D_{ec}\kappa_{ec}} \frac{D_{ec}\kappa_{ec} \cosh[\kappa_{ec}\ell] + D_c\kappa_c \sinh[\kappa_{ec}\ell]}{D_{ec}\kappa_{ec} \cosh[\kappa_{ec}(\ell + z_b)] + D_c\kappa_c \sinh[\kappa_{ec}(\ell + z_b)]} - \frac{\sinh[\kappa_{ec}z_0]}{D_{ec}\kappa_{ec}},$$

where $D_i = 1/[3(\mu'_{s,i} + \mu_{a,i})]$, $\kappa_i^2 = (D_i s^2 + \mu_{a,i} + 2\mu'_{s,i} k_0^2 F_i \tau)/D_i$, $z_b = 2D_{ec}(1 + R_{eff})/(1 - R_{eff})$, $z_0 = 3D_{ec}$, and R_{eff} and k_0 are defined in Section 2 (this solution assumes the top and bottom layers have the same optical index of refraction).

The two-layer weighting factors for a typical set of extra-cerebral/cerebral tissue properties are plotted in Fig. 4. Importantly, for a source-detector separation $\rho = 3$ cm, the change in the DCS optical density is more sensitive to changes in flow and absorption in the cerebral

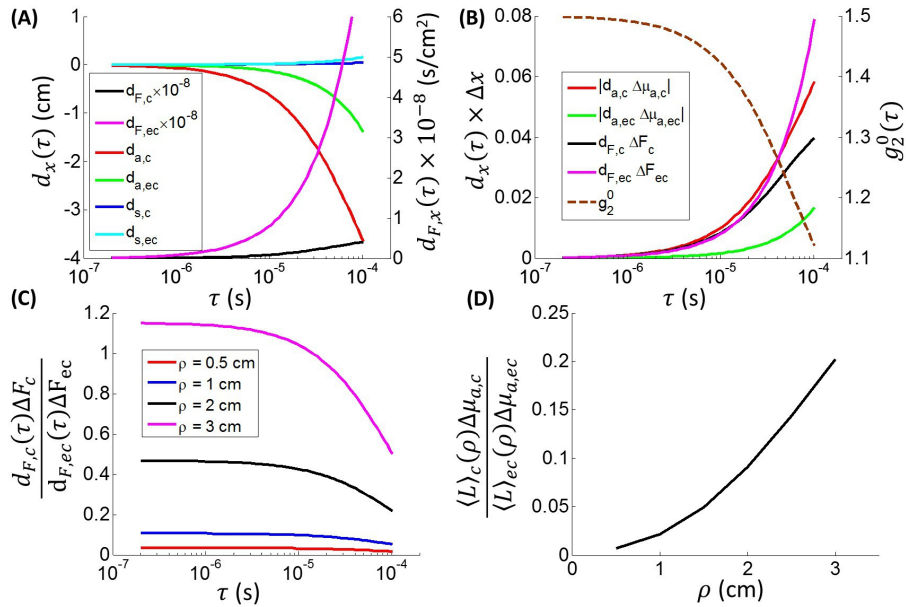


Fig. 4. **(A)** The two-layer multiplicative weighting factors (see Eq. (9)) for $d_{F,c}$ and $d_{F,ec}$ (right vertical-axis); and for $d_{a,c}$, $d_{a,ec}$, $d_{s,c}$, and $d_{s,ec}$. They are plotted as a function of the correlation time, τ , for source-detector separation, $\rho = 3$ cm, and optical wavelength, $\lambda = 785$ nm, given a set of typical extra-cerebral and cerebral tissue properties [51], i.e., $\mu_{a,c}^0 = 0.16$, $\mu_{a,ec}^0 = 0.12$, $\mu_{s,c}^0 = 6$, $\mu_{s,ec}^0 = 10$ cm $^{-1}$; $F_c^0 = 10^{-8}$, $F_{ec}^0 = 10^{-9}$ cm 2 /s; $\ell = 1$ cm, $n = 1.4$, and $n_{out} = 1$. **(B)** The two-layer DCS Modified Beer-Lambert components $d_{F,c}\Delta F_c$, $d_{F,ec}\Delta F_{ec}$, $|d_{a,c}\Delta\mu_{a,c}|$, and $|d_{a,ec}\Delta\mu_{a,ec}|$, plotted as a function of τ for a 10% increase in each parameter. On the right vertical-axis is the intensity autocorrelation function, $g_2^0(\tau)$, for $\beta = 0.5$. Notice that at shorter delay-times for $\rho = 3$ cm, the change in DCS optical density is equally sensitive to changes in cerebral blood flow, extra-cerebral blood flow, and cerebral absorption. The change in DCS optical density (OD_{DCS}) is less sensitive, however, to changes in extra-cerebral absorption. **(C)** The ratio of the cerebral (c) and extra-cerebral (ec) flow components in the DCS optical density perturbation, $\Delta OD_{DCS}(\tau)$ (Eq. (9)), for 4 separations, $\rho = 0.5, 1, 2,$ and 3 cm. These data are plotted as a function of τ assuming a 10% increase in cerebral and extra-cerebral blood flow. For the shorter separations of 0.5 and 1 cm, the ratio is substantially less than one; in this case, the DCS optical density is predominantly sensitive to the extra-cerebral layer. At the 3 cm separation, the DCS optical density is more sensitive to cerebral blood flow than extra-cerebral blood flow at the short delay-times, i.e., the ratio is greater than one. However, at longer delay-times, the ratio decreases. **(D)** The ratio of the cerebral and extra-cerebral absorption components in the two-layer Modified Beer-Lambert law for DOS/NIRS, plotted as a function of ρ for a 10% increase in cerebral and extra-cerebral absorption. $\langle L \rangle_c$ and $\langle L \rangle_{ec}$ are the cerebral and extra-cerebral partial pathlengths [18, 21]. Notice from panels (C) and (D) that the DCS optical density is more sensitive to the cerebral layer than the NIRS optical density is, consistent with findings in work of reference [59].

layer than in the extra-cerebral layer (except for at very long delay-times). This sensitivity is especially prominent at the shorter delay-times (Figs. 4(B), 4(C)). In practice the situation is helped by differences in magnitude of cerebral versus extra-cerebral flow (e.g., cerebral flow is quite often 10 times larger than extra-cerebral flow) [60]. We note here that the sensitivity to cerebral flow changes (Fig. 4(C)) depends on the specific ratio of cerebral to extra-cerebral flow [59]. For example, if $F_c^0 = 6F_{ec}^0$, the ratio of the cerebral flow component ($d_{F,c}\Delta F_c$) to extra-cerebral flow component ($d_{F,ec}\Delta F_{ec}$) is 0.7 at short delay-times for $\rho = 3$ cm (compared to 1.15 for $F_c^0 = 10F_{ec}^0$ in Fig. 4(C)). Further, this ratio depends on the extra-cerebral layer thickness, because the NIR light intensity is exponentially attenuated with increasing tissue depth. For example, if the extra-cerebral layer thickness is increased to $\ell = 1.1$ cm, then the ratio of the flow components in Fig. 4(C) at short delay-times is 0.8 for $\rho = 3$ cm.

The increase in the influence of the extra-cerebral layer at longer delay times (Fig. 4(C)) can be explained from consideration of the pathlengths of light, specifically their association with short versus long correlation decay times τ . Briefly, in the temporal autocorrelation function, long light paths contribute to rapid decays of the signal (short τ) and short light paths contribute to slow decays of the signal (large τ) [61, 62]. Short source-detector separations, e.g., $\rho = 0.5$ cm, mostly sample the superficial layer, and the DCS optical density perturbation is predominantly sensitive to the superficial layer in this case (Fig. 4(C)). Interestingly, a comparison of Figs. 4(C) and 4(D) reveals that the DCS optical density is more sensitive to cerebral changes than the DOS/NIRS optical density (consistent with findings of Selb *et al* [59]). Again, this effect arises in part because cerebral blood flow is much greater than extra-cerebral blood flow, and in part because DCS is effectively a time-resolved technique that permits separation of long light paths (shorter delay-times) from short light paths (longer delay-times) [59].

4. Results

4.1. Validation with simulated data

We tested the semi-infinite DCS Modified Beer-Lambert law (Eq. (4)) using simulated data (Fig. 5), as well as real data collected from a juvenile pig (Figs. 7, 8). The simulated DCS data was generated from semi-infinite analytical solutions of the correlation diffusion equation (Eq. (5)) with added noise [63]. Baseline tissue blood flow and optical properties in the simulated data were chosen to be representative of the head [64], and perturbations from baseline were induced by varying blood flow (F) from +50% to -50%, with constant tissue optical properties. Figure 5(A) shows the simulated intensity autocorrelation functions for these baseline and perturbed conditions, plotted as a function of delay-time. The DCS Modified Beer-Lambert law (Eq. (4)) was then applied to this simulated data set to calculate the flow change as a function of delay-time (Fig. 5(B)). Good agreement between the calculated and actual flow changes is found for a wide range of delay-times.

We next quantified the range of delay-times for which the DCS Modified Beer-Lambert law can be accurately employed. First, recall that the semi-infinite DCS Modified Beer-Lambert law is expected to be accurate in the limit $2\mu'_s k_0^2 F \tau / \mu_a \ll 1$ (Appendix 2). The simulations show that it will remain fairly accurate even when $2\mu'_s k_0^2 F \tau / \mu_a \sim 1$. In order to appreciate the simulation results more generally, we introduce the dimensionless delay-time, $\tau \gamma^0 F^0$, which depends on baseline blood flow (F^0), correlation time-delay (τ), and $\gamma^0 \equiv K_0^0 (\mu_s^0 / \mu_a^0) k_0^2 r_1^0$ (see Eq. (B.4)). When this dimensionless delay-time is ~ 1 , then the baseline electric field autocorrelation function has decayed by $\sim 1/e$. In terms of this dimensionless delay-time, the limit $2\mu'_s k_0^2 F \tau / \mu_a \ll 1$ corresponds to the baseline condition $\tau \gamma^0 F^0 \ll \alpha$, where $\alpha \equiv \gamma^0 \mu_a^0 / (2\mu_s^0 k_0^2)$. For the “typical” conditions chosen for Fig. 5, $\alpha = 2.3$.

Figure 5(B) plots the calculated DCS Modified Beer-Lambert flow change for each

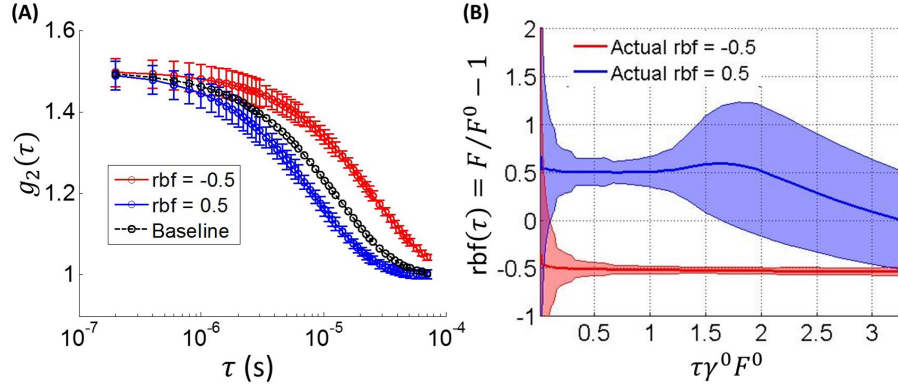


Fig. 5. **(A)** Simulated semi-infinite intensity autocorrelation curves (mean \pm SD across $N = 10k$ curves) plotted as a function of the delay-time τ for a -50% and $+50\%$ change in flow while tissue optical properties were held constant. The source-detector separation, light wavelength, and baseline tissue properties are $\rho = 3$ cm, $\lambda = 785$ nm, and $\mu_a^0 = 0.1$ cm $^{-1}$, $\mu_s^0 = 8$ cm $^{-1}$, $F^0 = 10^{-8}$ cm 2 /s, $n = 1.4$, $n_{out} = 1$, respectively. The simulated DCS data were generated from the semi-infinite solution of the correlation diffusion equation (Eq. (5)) with added noise derived from a correlation noise model [63]. The correlation noise model was evaluated at a baseline DCS intensity of $50k$ photons a second and an averaging time of 2.5 seconds. **(B)** Fractional blood flow changes (mean \pm SD) estimated by applying the semi-infinite DCS Modified Beer-Lambert law, i.e., $rbf(\tau) = \Delta OD_{DCS}(\tau)/(d_F(\tau)F^0)$ (Eq. (4)), to the simulated data. To appreciate the simulated results more generally, these fractional blood flow changes are plotted against the dimensionless delay-time $\tau\gamma^0 F^0$. Here, $(\gamma^0 F^0)^{-1}$, where $\gamma^0 \equiv K_0^0(\mu_s^0/\mu_a^0)k_0^2 r_1^0$ (see Eq. (B.4)), is approximately the characteristic decay time of the baseline electric field autocorrelation function (see Appendix 2).

dimensionless delay-time. The difference (error) between the calculated flow change and the true flow change (simulated value) is relatively small, even for dimensionless delay-times approaching $\alpha = 2.3$. We also see that for a 50% increase in flow, the DCS Modified Beer-Lambert law is accurate over a narrower range of dimensionless delay-time than for a 50% decrease (Fig. 5(B)). The latter behavior is a consequence of the fact that when flow is increased, the intensity autocorrelation function decays more rapidly. When the autocorrelation curves are close to fully decayed, then the DCS Modified Beer-Lambert law is predominantly sensitive to correlation noise instead of flow. For a perturbed state from baseline (e.g., $rbf = 50\%$), the limit $2\mu_s^0 k_0^2 F \tau / \mu_a \ll 1$ corresponds to $\tau\gamma^0 F^0 \ll \alpha(F^0/F)$ (assuming constant optical properties). Thus, a larger value of F reduces the value of the dimensionless delay-time upper limit.

4.2. Noise consideration

At very short delay-times, there is little difference between the intensity autocorrelation curves corresponding to different blood flows (Fig. 5(A)). In this limit, the changes to the DCS optical density are heavily influenced by correlation noise, and flow calculations at the very short delay-times in Fig. 5(B) are noisy. In general, from applying error propagation rules to Eq. (4), the noise in the calculated flow change ($\delta(rbf(\tau))$) as a function of τ for constant tissue optical properties is

$$\delta(rbf(\tau)) = \frac{1}{d_F(\tau)F^0} \delta(\Delta OD_{DCS}(\tau)) = \frac{1}{d_F(\tau)F^0} \frac{\delta(g_2(\tau) - 1)}{|g_2(\tau) - 1|}. \quad (10)$$

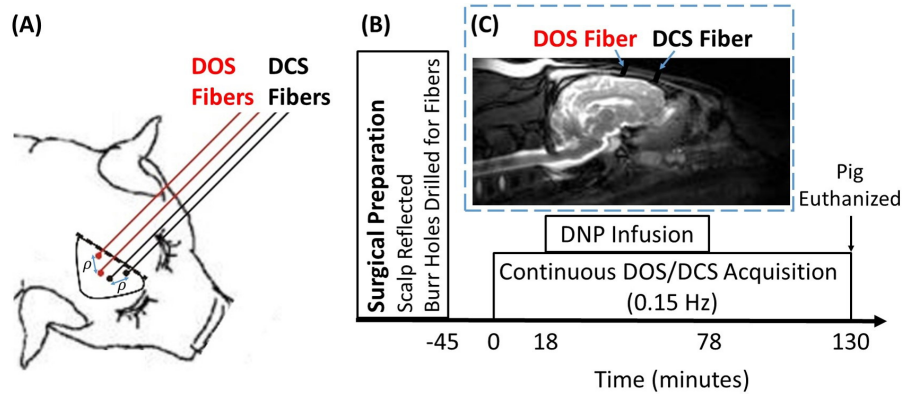


Fig. 6. (A) To monitor hemodynamics in the semi-infinite geometry, a juvenile pig's scalp was reflected, and 2.5 mm burr holes were drilled through the skull for placement of 90-degree optical fibers. A DOS/NIRS source-detector pair (red circles) measured cerebral tissue absorption, and a DCS source-detector pair (black circles) measured cerebral blood flow. The source-detector separation of both pairs is $\rho \approx 1.5$ cm. (B) Schematic showing the timeline of the experiment in minutes. Venous infusion of dinitrophenol (DNP, 9 mg/kg) dramatically stimulated cerebral oxygen metabolism and induced a 200% increase in cerebral blood flow. The DCS and DOS techniques were interleaved to measure blood flow and tissue absorption every 7 seconds. (C) Anterior-posterior slice of an anatomical MRI scan of a pig with similar weight to the juvenile pig used in this measurement. The burr holes for the two optical fibers closest to the midline in panel (A) have been artificially overlaid on this scan.

A correlation noise model can be used to accurately estimate $\delta(g_2(\tau) - 1)$ [63]. As τ increases, the correlation noise decreases, and $d_F(\tau)F_0$ increases (Fig. 2(A)). Both trends reduce the noise in rbf . However, when $|g_2(\tau) - 1|$ goes to zero as τ increases, an accompanying increase in noise is expected. From Fig. 5(B), the noise in rbf falls with increasing delay-time and then levels off around $\tau\gamma^0 F^0 \approx 0.3$; the noise then remains constant for a large range of delay-times.

As one would expect, the flow change computed with a single τ in the DCS Modified Beer-Lambert law is more sensitive to noise than the flow change extracted from nonlinear fits to the semi-infinite correlation diffusion solution across many delay-times. To ameliorate sensitivity to noise, multiple delay-times can also be used for the DCS Modified Beer-Lambert law. Then Eq. (4) becomes a system of linear equations, i.e., one equation for each delay-time, which can very rapidly be solved to derive flow changes.

4.3. In-vivo validation

Finally, we validated the semi-infinite DCS Modified Beer-Lambert law *in-vivo*. In this case, the scalp of a juvenile pig was reflected and 2.5-mm burr holes were drilled through the skull down to the dura (Fig. 6). Optical fibers were inserted into the holes to comprise a single DCS source-detector pair for measurement of cerebral blood flow, and a single DOS/NIRS source-detector pair for measurement of cerebral tissue absorption (Fig. 6(A)). The source-detector separations of both pairs were approximately 1.5 cm, and the baseline cerebral optical properties of the pig were assumed to be $\mu_a^0(785 \text{ nm}) = 0.2$ and $\mu_s^0(785 \text{ nm}) = 8 \text{ cm}^{-1}$ [65]. Importantly, in this measurement the semi-infinite geometry is a good approximation for the true tissue geometry, because the optical fibers are very close to the brain.

Figure 6(B) is a schematic showing the timeline of the experiment. While monitoring with

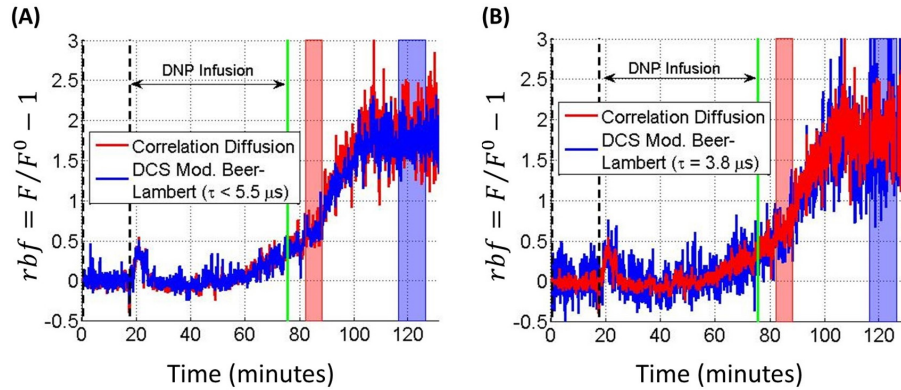


Fig. 7. Temporal fractional cerebral blood flow changes induced by injection of the drug dinitrophenol (DNP) in a juvenile pig. The baseline flow is $F^0 = 5.34 \times 10^{-8} \text{ cm}^2/\text{s}$, which is the average blood flow index over the 18 minute time interval between the vertical dashed lines. Cerebral blood flow changes were calculated from nonlinear fits to the semi-infinite correlation diffusion solution (Eq. (5)) and from the semi-infinite DCS Modified Beer-Lambert law (Eq. (4)) using (A) multiple delay-times, i.e., $\tau < 5.5 \mu\text{s}$, which corresponds to $g_2^0(\tau) > 1.25$, and (B) a single delay-time, i.e., $\tau = 3.8 \mu\text{s}$, which corresponds to $g_2^0(\tau) = 1.3$. Measured tissue absorption changes (Fig. 8(B)) were incorporated in both the correlation diffusion fit and the DCS Modified Beer-Lambert law. Tissue scattering was assumed to remain constant at $\mu_s' = 8 \text{ cm}^{-1}$, and the red and blue shaded regions indicate quasi steady-state temporal intervals that are analyzed further in Fig. 8.

DOS and DCS, a 200% increase in cerebral blood flow was induced in the pig via venous infusion of 9 mg/kg of the drug dinitrophenol (DNP). DNP is a proton transporter across cell membranes which disrupts the mitochondrial proton gradient [66]. In an effort to restore the proton gradient, cells stimulate cerebral oxygen metabolism [66], which in turn leads to a large increase in cerebral blood flow. Additional details about the animal preparation and measurement are in *Appendix 3*.

The calculated temporal cerebral blood flow changes in the pig (due to DNP) using the DCS Modified Beer-Lambert law are in good agreement with the calculated changes from nonlinear fits to the semi-infinite solution of the correlation diffusion equation (Fig. 7). Measured cerebral absorption changes (Fig. 8(B)) were incorporated in the blood flow calculations. Note, when using multiple delay-times in the DCS Modified Beer-Lambert law, the noise in temporal blood flow estimates is comparable to the nonlinear diffusion fit (Fig. 7(A)). For single τ blood flow monitoring, the temporal blood flow noise is larger, but the average blood flow changes are the same (Fig. 7(B)); this behavior demonstrates the feasibility of accurate single τ blood flow monitoring with DCS. In Fig. 7(B), the dimensionless delay-time $\tau\gamma^0 F^0 = 0.33$ (corresponding to $g_2^0(\tau) = 1.3$) was used for single delay-time monitoring.

The estimated cerebral blood flow changes from the DCS Modified Beer-Lambert law are also plotted as a function of dimensionless delay-time in Fig. 8(A) for two quasi steady-state temporal intervals. During these temporal flow intervals, the blood flow changes were also determined from nonlinear fits to the semi-infinite correlation diffusion solution. The average blood flow changes from the nonlinear fit estimates are 185% and 64% (solid black lines). The horizontal dashed lines in Fig. 8(A) indicate the noise in the nonlinear fit estimates of blood flow (constant because the nonlinear correlation diffusion fit uses all delay-times). Note that the average value of the DCS Modified Beer-Lambert law estimate of the larger flow increase is within the noise of the nonlinear correlation diffusion fit estimate for the delay-time interval

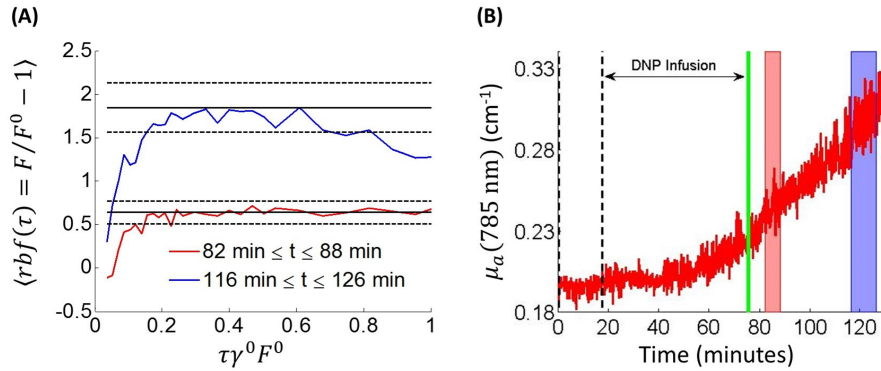


Fig. 8. (A) Mean fractional cerebral blood flow changes (averaged across indicated time intervals in the legend) as a function of the dimensionless delay-time $\tau \gamma^0 F^0$ (see Fig. 5 caption) in a juvenile pig. (B) The pig's cerebral absorption over time, which was calculated from applying the semi-infinite Modified Beer-Lambert law (Eq. (1)) to the measured DOS/NIRS intensity changes from baseline. Note that the shaded regions in panel (B) indicate the temporal intervals averaged over in panel (A). The cerebral blood flow changes in panel (A) were obtained from applying the semi-infinite DCS Modified Beer-Lambert law (Eq. (4)) to the measured intensity autocorrelation curves and the measured cerebral absorption changes. The horizontal solid and dashed black lines in panel (A) indicate the fractional blood flow changes (Mean \pm SD) obtained from fitting the intensity autocorrelation curves to the non-linear semi-infinite correlation diffusion solution (Eq. (5)).

$0.16 < \tau \gamma^0 F^0 < 0.82$, which corresponds to the baseline intensity autocorrelation function range $1.15 < g_2^0(\tau) < 1.40$. The smaller flow increase in Fig. 8(A) is accurate for an even wider range of delay-times, because the intensity autocorrelation function associated with this increase requires a longer delay-time to completely decay (see *Section 4.1*).

5. Discussion

The Modified Beer-Lambert approach has been employed extensively in the biomedical optics community [2, 7, 67–70], in large part because of its simplicity. With this approach, researchers have monitored temporal changes in blood oxygenation and blood volume with CW light, using only one source-detector separation. In the present paper, we have extended the Modified Beer-Lambert approach to the DCS measurement, and we have demonstrated the accuracy of this extension in both simulations (Fig. 5) and *in-vivo* data (Figs. 7, 8). The DCS Modified Beer-Lambert approach offers some advantages compared to the traditional analysis scheme of fitting intensity autocorrelation data to nonlinear solutions of the correlation diffusion equation.

5.1. Real-time estimates of blood flow changes

The DCS Modified Beer-Lambert law is a linear equation relating changes in blood flow to changes in signal for *any* tissue geometry. Although the correlation diffusion solution in the semi-infinite geometry is closed form, the correlation diffusion solutions in more intricate geometries (e.g., curved, layered) are vastly more complex, and consequentially quite time-consuming when fitting data. With the DCS Modified Beer-Lambert approach, the correlation diffusion solutions are needed only once to evaluate the multiplicative weighting factors at the “baseline” tissue state, e.g., Eq. (A.3). We emphasize that even for geometries where closed form solutions are not available, these multiplicative weighting factors can still be evaluated

numerically. Then, blood flow changes from baseline are rapidly determined by solving a linear equation (Eq. (4) or (8)). Consequentially, the DCS Modified Beer-Lambert law is well suited for real-time blood flow monitoring, especially in tissue geometries that are not semi-infinite.

5.2. *Blood flow monitoring in tissues wherein light propagation is non-diffusive*

Diffusive light transport is not required for using the DCS Modified Beer-Lambert approach. In blood flow monitoring applications wherein the photon diffusion model is not valid, the multiplicative weighting factors can be evaluated using solutions of the correlation transport equation [71, 72] instead of the correlation diffusion equation (see *Appendix 1*). For the tissue geometry of interest, the correlation transport equation can be solved numerically with Monte Carlo techniques [15, 61]. Thus, the DCS Modified Beer-Lambert approach facilitates accurate blood flow monitoring for the small source-detector separations typical of endoscopic probes, for complex tissues that contain “non-diffusing” domains such as (arguably) cerebral spinal fluid inside the head [73–75], and for tissues that contain very high concentrations of blood, as in the liver [76]. In all three of these examples, the assumptions underlying the photon diffusion model are violated, and therefore the photon diffusion model is not expected to be accurate. Another potential application of the non-diffusive DCS Modified Beer-Lambert approach is blood flow monitoring with visible light.

5.3. *Improved depth sensitivity*

The DCS Modified Beer-Lambert law permits blood flow monitoring with intensity autocorrelation measurements at a single delay-time, in contrast to the traditional correlation diffusion approach wherein blood flow estimates are obtained by acquiring and fitting a full, nearly continuous, intensity autocorrelation curve. It is now well established that the autocorrelation function decay times associated with long light paths are relatively short, while the decay times associated with short light paths are relatively long [59, 61, 62]. Thus, the autocorrelation function at shorter delay-times will be inherently more sensitive to deeper tissues in remission geometries (Fig. 4), which in turn means that the sensitivity of the DCS measurement to blood flow at deeper tissue depths is improved by using short delay-times in the DCS Modified Beer-Lambert law. Conversely, using long delay-times improves the sensitivity of the DCS measurement to tissue blood flow at shallow depths. This same effect can be achieved by fitting different parts of the intensity autocorrelation curve to the correlation diffusion model. In practice, these correlation diffusion fits still require several delay-times spanning a significant portion of the autocorrelation curve. By using a single delay-time, the experimenter has finer control of the measurement depth sensitivity for DCS measurements. Note that for DCS measurements in transmission geometries [77], the autocorrelation function at longer delay-times (short light paths) will be more sensitive to tissue adjacent to the straight line between source and detector.

5.4. *Increased temporal resolution of DCS measurements*

The DCS Modified Beer-Lambert law offers new routes for increased DCS measurement speed and for simpler instrumentation. Underlying these advantages is again blood flow monitoring with a single delay-time. We and others have used multiple- τ hardware correlators to measure the intensity autocorrelation function [78, 79] at delay-times spanning several orders of magnitude from ~ 100 ns to ~ 10 ms. Achieving sufficient SNR for deep tissue DCS measurements (e.g., as in the brain) typically requires averaging many ($N > 100$) of these 10-ms autocorrelation curves. The single delay-time cerebral blood flow monitoring in the pig shown in Fig. 7(B) was done at $\tau = 3.8 \mu\text{s}$. Thus, in this example, ~ 250 blood flow measurements can be acquired in 1 ms, which can then be temporally averaged to reduce noise. In 10 ms, which is

roughly the time required to measure a single autocorrelation curve with a multiple- τ correlator, ~ 2500 blood flow measurements can be acquired and averaged. Therefore, even though single- τ blood flow monitoring with the DCS Modified Beer-Lambert law is more sensitive to correlation noise than multiple- τ monitoring (Fig. 7), the substantial improvement in the blood flow sampling rate with single- τ monitoring means that enough averaging can be employed to compensate for this additional noise while still maintaining high DCS measurement speeds. Blood flow measurements at high acquisition rates are advantageous in several applications, including schemes to filter out motion artifacts in exercising muscle [80]. Single- τ monitoring also makes it possible to use single- τ hardware correlators, which are cheaper than multiple- τ hardware correlators. Alternatively, software correlators [78] for a single delay-time could be implemented.

5.5. *Filtering contamination from superficial tissues in deep tissue flow monitoring*

The same paradigms that have been developed with the Modified Beer-Lambert law to filter contamination from superficial tissues in blood oxygenation measurements of the tissue of interest (e.g., the brain) [20–22, 81, 82] can also be used in the DCS Modified Beer-Lambert formulation for blood flow monitoring. In fact, these paradigms are likely to work even better with DCS, because DCS is more sensitive to deep brain hemodynamics than continuous-wave DOS/NIRS (Figs. 4C, 4D) [59].

Building on work done with the DOS/NIRS Modified Beer-Lambert law [21, 22], a useful scheme for filtering superficial tissue contamination in the DCS signal is to employ two source-detector separations. One source-detector separation should be long and the other short. Detected light from the long separation travels through both superficial and deep layers of tissue, but detected light at the short separation is predominantly confined to the superficial layer. Two two-layer DCS Modified Beer-Lambert law equations (corresponding to the two source-detector separations) can then be employed to better isolate the deep tissue blood flow component from the superficial blood flow component. Ideally the experimenter would acquire “initial/baseline” measurements wherein only superficial blood flow is changing.

In cerebral monitoring, one way to change superficial blood flow without affecting cerebral blood flow is to vary the pressure of the optical probe against the head [83]. Initial measurements acquired during probe pressure modulation can then be used to derive the patient-specific weighting factors in the DCS Modified Beer-Lambert law. These weighting factors would subsequently be used to filter superficial contamination in cerebral blood flow monitoring. We will develop this idea further in a future paper.

6. Conclusion

The Modified Beer-Lambert extension to the DCS measurement is accurate enough to be useful for blood flow monitoring. It facilitates real-time flow monitoring in complex tissue geometries, provides a novel route for increasing DCS measurement speed, and can be used to probe tissues wherein light transport is non-diffusive. It also can be used to filter signals from superficial tissues.

A. Appendix 1

The multiplicative weighting factors d_F , d_a , and d_s in Eq. (4) can be estimated by taking the appropriate derivative of the solutions to the correlation diffusion equation applied to the appropriate geometry (e.g., semi-infinite homogeneous, etc.). First, using the Siegert relation,

we have:

$$\begin{aligned} d_F(\tau, \rho) &\equiv \frac{\partial OD_{DCS}^0}{\partial F} = \frac{\partial}{\partial F} [-\log(g_2^0(\tau, \rho) - 1)] = \frac{\partial}{\partial F} [-\log(\beta [g_1^0(\tau, \rho)]^2)] \\ &= \frac{\partial}{\partial F} [-\log(\beta) - 2\log(g_1^0(\tau, \rho))] = 2 \frac{\partial}{\partial F} [-\log(g_1^0(\tau, \rho))]. \end{aligned} \quad (A.1)$$

Similarly,

$$\begin{aligned} d_a(\tau, \rho) &= 2 \frac{\partial}{\partial \mu_a} [-\log(g_1^0(\tau, \rho))], \\ d_s(\tau, \rho) &= 2 \frac{\partial}{\partial \mu'_s} [-\log(g_1^0(\tau, \rho))]. \end{aligned} \quad (A.2)$$

Here, $g_1(\tau, \rho)$ is the solution to the correlation diffusion equation for the geometry of interest [1, 15], and the derivatives of the solution are evaluated at baseline conditions. In conditions where an analytical solution for the correlation diffusion equation does not exist, the multiplicative weighting factors can be computed numerically:

$$\begin{aligned} d_F(\tau, \rho) &= \frac{2}{\Delta F} \log \left(\frac{g_1(\tau, \rho, F^0 - \Delta F/2, \mu_a^0, \mu_s'^0)}{g_1(\tau, \rho, F^0 + \Delta F/2, \mu_a^0, \mu_s'^0)} \right), \\ d_a(\tau, \rho) &= \frac{2}{\Delta \mu_a} \log \left(\frac{g_1(\tau, \rho, F^0, \mu_a^0 - \Delta \mu_a/2, \mu_s'^0)}{g_1(\tau, \rho, F^0, \mu_a^0 + \Delta \mu_a/2, \mu_s'^0)} \right), \\ d_s(\tau, \rho) &= \frac{2}{\Delta \mu'_s} \log \left(\frac{g_1(\tau, \rho, F^0, \mu_a^0, \mu_s'^0 - \Delta \mu'_s/2)}{g_1(\tau, \rho, F^0, \mu_a^0, \mu_s'^0 + \Delta \mu'_s/2)} \right), \end{aligned} \quad (A.3)$$

where $\Delta F/F^0 = \Delta \mu_a/\mu_a^0 = \Delta \mu'_s/\mu_s'^0 = 10^{-5}$. Equations (A.1), (A.2), and (A.3) are important intermediate results, which provide generalized expressions for the analytical and numerical computation of the multiplicative weighting factors in the DCS Modified Beer-Lambert law for any homogeneous geometry.

Evaluating these equations requires knowledge of the baseline tissue optical properties and the baseline flow index. The baseline flow index can be obtained from a nonlinear fit of the baseline intensity autocorrelation curve to the correlation diffusion solution (see *Section 2*). The baseline tissue optical properties can either be assumed from the literature (e.g., [76]) or measured with time-domain or frequency-domain DOS/NIRS [47, 48]. For typical tissue measurements wherein scattering does not change, the sensitivity in the computed fractional blood flow change to assumed baseline optical properties is small (Fig. 9). For the example of flow changes shown in Fig. 9, $\pm 50\%$ errors in the assumed baseline optical properties affected the estimated fractional flow change by only ± 5 percentage points (e.g., from 0.50 to 0.45). Thus, for many applications, errors in the assumed baseline optical properties have little effect on calculated changes in blood flow. Computed fractional flow changes are a little more sensitive to errors in baseline flow than to errors in baseline optical properties. Specifically, for the example of flow changes in Fig. 9, $\pm 10\%$ errors in baseline flow affected the estimated fractional flow change by ± 5 percentage points, and $\pm 25\%$ errors in baseline flow affected the estimated fractional flow change by ± 10 percentage points (results not shown).

An important assumption in this approach is that the correlation diffusion equation accurately models the electric field autocorrelation function in tissue. This assumption is valid when using large source-detector separations, $\rho \gg 1/(\mu_a + \mu'_s)$, to measure highly scattering media with isotropic dynamics [15]. The DCS Modified Beer-Lambert law, Eq. (4), however, can also be used for correlation transport conditions wherein the correlation diffusion equation

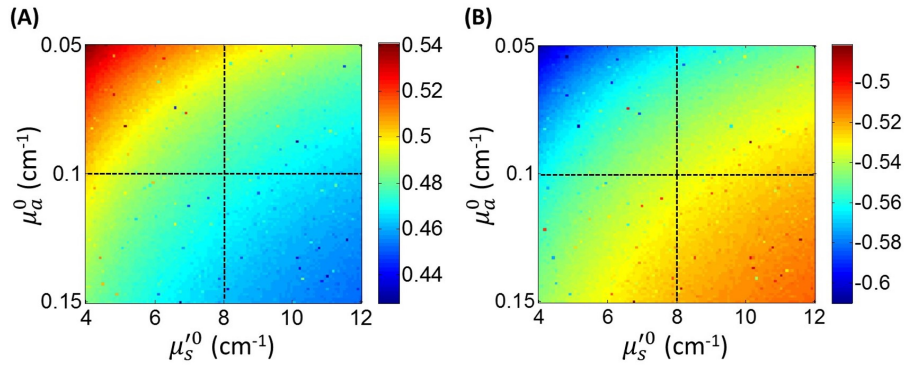


Fig. 9. Fractional blood flow changes (i.e., $F/F^0 - 1$) computed from applying the semi-infinite DCS Modified Beer-Lambert law (Eq. (4)) with assumed baseline optical properties of μ_a^0 (vertical axis) and μ_s^0 (horizontal axis) to semi-infinite simulated data with noise ($N = 1k$ curves). The actual blood flow and absorption changes are (A) 50% and 15%, and (B) -50% and -15%, respectively. Tissue scattering was constant, and the actual baseline properties (including simulated noise parameters) are identical to those in Fig. 5, e.g., $\mu_a^0 = 0.1$, $\mu_s^0 = 8 \text{ cm}^{-1}$ (denoted by dashed lines). To compute the absorption changes from the simulated data, the Modified Beer-Lambert law (Eq. (1)) was employed. The differential pathlength ($\langle L \rangle$) in Eq. (1) was calculated from the assumed baseline optical properties [84]. Finally, the baseline flow index, F^0 , was extracted from a nonlinear fit of the simulated baseline data to the semi-infinite correlation diffusion solution (Eq. (5)) evaluated at the assumed baseline optical properties. Errors in the assumed baseline optical properties only have small effects on the computed fractional flow change. Note that the computed fractional blood flow changes are not exactly 50% and -50% when the exact optical properties are assumed because of small errors arising from truncating the tissue absorption terms in the Taylor Series expansion of the DCS optical density (Eq. (3)) to first order.

breaks down. In this case, the derivatives in Equations (A.1) and (A.2) will have to be applied to the solutions of the so-called correlation transport equation [71, 72], which can be solved numerically with Monte Carlo techniques [15, 61].

B. Appendix 2

The semi-infinite solution to the correlation diffusion equation (Eq. (5)) is approximately exponential in the small delay-time limit, i.e., $g_1(\tau) \approx \exp(-\gamma F \tau)$, with $\gamma \equiv K_0(\mu'_s/\mu_a)k_0^2 r_1$. Normalizing the delay-time by the characteristic decay-time, i.e., $\tau_c = (\gamma F)^{-1}$, is a meaningful dimensionless way to express delay-times (Figs. 5, 8), e.g., $g_1 \approx 0.4$ for $\tau\gamma F = 1$. Further, the DCS Modified Beer-Lambert law (Eq. (4)) is a good approximation in the small delay-time limit because $-\log(g_2(\tau) - 1) = -\log(\beta g_1^2) = 2\gamma\tau F - \log(\beta)$ is linear with respect to F . To derive the small delay-time limit of the semi-infinite correlation diffusion solution, first note that if the source-detector separation, ρ , is much greater than the photon transport mean-free path through tissue, ℓ_{tr} , then (see Eq. (2))

$$\begin{aligned} r_b &\approx r_1(1 + x/r_1^2), \\ \frac{1}{r_b} &\approx \frac{1}{r_1} \left(1 - \frac{x}{r_1^2}\right), \end{aligned} \quad (\text{B.1})$$

where $x \equiv 2z_b(z_b + \ell_{tr})$. Substituting Eq. (B.1) into Eq. (2), we see that

$$G_1(\tau) = \frac{3}{4\pi\ell_{tr}} \frac{\exp(-K(\tau)r_1)}{r_1} \left[1 - \exp\left(\frac{-K(\tau)x}{r_1}\right) \left(1 - \frac{x}{r_1^2}\right)\right]. \quad (\text{B.2})$$

In the limit $K(\tau)x/r_1 \ll 1$, which is satisfied at small delay-times, Eq. (B.2) simplifies further to

$$G_1(\tau) \approx \frac{3}{4\pi\ell_{tr}} \frac{x \exp(-K(\tau)r_1)}{r_1^2} \left(K(\tau) + \frac{1}{r_1}\right). \quad (\text{B.3})$$

In the more stringent limit $2(\mu'_s/\mu_a)k_0^2 F \tau \ll 1$, the electric field autocorrelation function in Eq. (B.3) is approximately exponential:

$$g_1(\tau) = \frac{G_1(\tau)}{G_1(0)} \approx \exp(-\gamma F \tau) \left(1 + \frac{\gamma F \tau}{r_1 K_0 + 1}\right) \approx \exp(-\gamma F \tau), \quad (\text{B.4})$$

where $\gamma = K_0(\mu'_s/\mu_a)k_0^2 r_1$ and $K_0 \equiv K(0) = [3\mu_a(\mu_a + \mu'_s)]^{1/2}$.

C. Appendix 3

All animal procedures were in accordance with guidelines established by the National Institutes of Health and approved by the Institutional Animal Care and Use Committee of the University of Pennsylvania. Diffuse optical measurements were performed on a male Yorkshire juvenile pig (28 kg). The animal was anesthetized with an initial intramuscular injection of ketamine (25 mg/kg), dexmedetomidine (0.025 mg/kg), and glycopyrolate (0.02 mg/kg), intubated, and then mechanically ventilated with a mixture of $\sim 3\%$ isoflurane in pure oxygen gas. To prepare for hemodynamic monitoring in the semi-infinite geometry, the pig's scalp was reflected over the left hemisphere of the brain, and a dental drill was used to form 2.5 mm burr holes through the skull down to the dura for the placement of optical fibers (see Fig. 6). One DCS source-detector pair and one DOS/NIRS source-detector pair were used for hemodynamic monitoring. The positions of these fibers, denoted as (lateral distance from the center of the eye, lateral distance from midline), are (10 mm, 5 mm), (21 mm, 15 mm), (26 mm, 15 mm), and (37 mm, 5 mm) for the DCS source, DCS detector, DOS/NIRS source, and DOS/NIRS detector, respectively. Thus, the source-detector separations for both the DOS/NIRS and DCS pairs are approximately 15 mm.

Upon completion of the surgical preparation, the ventilation of the pig was switched to a mixture of oxygen and nitrogen (3:7) with no isoflurane. Anesthesia was maintained instead

with intravenous administration of ketamine (20-60 mg/kg/h). Throughout the rest of the study, arterial oxygen saturation and end-tidal CO₂ were continually monitored with blood gas samples from the femoral artery and with a capnograph, respectively. The ventilation rate was initially adjusted to maintain an end-tidal CO₂ between 40 and 50 mm Hg.

After inserting ninety-degree bend terminated optical fibers (Fiberoptic Systems, Simi Valley, CA) in the burr holes, a 5-pound sandbag weight was carefully placed on top of the fibers to secure them in place. Two 1-mm diameter multi-mode borosilicate fibers (Fiberoptic Systems) delivered source light to the cerebral tissue, and a third 1-mm diameter multi-mode fiber received diffusing light from the tissue for DOS/NIRS detection. For DCS detection, a 4 × 1 bundle of 780HP single-mode fibers (Fiberoptic Systems) was used. These fibers interfaced to a portable custom-built instrument designed for hemodynamic monitoring, which is described in detail elsewhere [85, 86]. In the DCS measurement, a continuous wave, long coherence length 785 nm laser (CrystaLaser Inc., Reno, NV) was employed to deliver source light, and the outputs from an array of 4 high sensitivity avalanche photodiodes (SPCM-AQ4C, Excelitas, Canada) operating in photon counting mode were connected to a multiple- τ hardware correlator (Correlator.com, Bridgewater, NJ). In the DOS/NIRS measurement, three lasers (690 nm, 785 nm, 830 nm; OZ Optics, Canada) intensity modulated at 70 MHz were coupled to an optical switch (DiCon Fiberoptics, Richmond, CA), which sequentially cycled the source light between the three wavelengths. A heterodyne detection scheme using a photomultiplier tube (R928, Hamamatsu, Bridgewater, NJ) was employed for DOS/NIRS detection. The data acquisition was interleaved between DOS/NIRS and DCS to measure blood flow and blood oxygenation with a sampling rate of 0.15 Hz.

After ten minutes of baseline cerebral hemodynamic monitoring in the pig, the drug dinitrophenol (DNP, 9mg/kg) was injected intravenously over an hour to dramatically increase cerebral oxygen metabolism and blood flow [66] (see Fig. 6(B)). The oxygen content in the ventilated gas was increased as needed to maintain the arterial oxygen saturation in the pig above 95%. Ketamine was also supplemented as needed with boluses of diazepam (0.1-0.2 mg/kg) to ensure adequate sedation as the oxygen metabolism increased. After two hours of hemodynamic monitoring, the pig was euthanized with pentobarbital.

Acknowledgments

We gratefully acknowledge help from Marion Knaus and Victoria Pallett per preparing the pig, and we thank longtime collaborators Daniel Licht, John Detre, Emile Mohler, Thomas Floyd, Turgut Durduran, and Theresa Busch for valuable discussions. We acknowledge support from the National Institutes of Health (R01-NS060653, NHLBI-HL007915, 8P41-EB015893), the American Heart Association (ABP, 14POST20460161), the Thrasher Pediatric Research Foundation Early Career Award (DRB), and the São Paulo Research Foundation (RCM, 2012/02500-8, 2013/07559-3).